# Simultaneous Radar Detection and Frequency Measurement by Broadband Microwave Photonic Processing

Jingzhan Shi, Fangzheng Zhang, *Senior Member, IEEE*, De Ben, and Shilong Pan, *Senior Member, IEEE, Fellow, OSA*

***Abstract*—Incorporating radar detection and frequency measurement functions within a single system is highly desirable in modern RF applications. In this article, a microwave photonic system is proposed and demonstrated to simultaneously realize broadband radar detection and frequency measurement. By sharing a light with ± 2nd-order linear frequency-modulated (LFM) sidebands in a polarization-division-multiplexing manner, radar detection and frequency measurement functions can be realized simultaneously. In the transmitter, the shared light is used to generate a radar signal that has a quadrupled bandwidth compared with the input electrical LFM signal. In the receiver, the shared light is applied as the reference to perform photonic de-chirping of the radar echo and to scan the frequency of the signal under test (SUT) along two orthogonal polarization directions. In the experiment, a 4.5–6.5 GHz LFM signal is used to generate the shared light source, based on which radar detection (bandwidth: 18–26 GHz) with a range resolution as high as 2.06 cm, and frequency measurement (measurement range: 28–36 GHz) with a scanning rate of 0.8 GHz/$\mu$s and a resolution of 37.6 MHz are achieved. In addition, the reconfigurablilty of the frequency measurement range, and its capability for measuring the multi-tone and wideband signals are also demonstrated.**

***Index Terms*—Microwave frequency measurement, microwave photonics, polarization-division multiplexing, radar detection.**

## I. Introduction

MICROWAVE photonics (MWP) uses photonic techniques to generate, distribute, process, and analyze microwave or radio frequency (RF) signals. MWP has attracted lots of attention because of its advantages including high frequency, large bandwidth, low-loss transmission, and resistance to electromagnetic interference [1]–[3], etc. In the past few decades, MWP in communication systems, especially the radio-over-fiber (ROF) technique [4], has been extensively investigated. Recently, an increasing number of attentions have been paid to MWP applications in radar and electronic warfare (EW) systems [5]–[7], aiming to overcome the bandwidth limitations of traditional electric systems.

Previously, several MWP radar architectures have been proposed [8]–[18]. In [8], an MWP radar is demonstrated using a mode-locked-laser (MLL) to generate the transmit signal by photonic heterodyning, and to sample the radar echo with a photonic analog-to-digital converter (ADC). In another MWP radar, optical chirp to electrical chirp conversion is applied in the transmitter and a time-stretched ADC is used in the receiver [9]. Besides, MWP radar with de-chirp receiving is also proposed [10]–[12]. In [12], a broadband linear frequency modulated (LFM) signal is generated by an MWP frequency quadrupler, enabling a very high range resolution detection. The received radar echo is de-chirped by an MWP frequency mixer, which helps to reduce the sampling rate of the ADC and ensures a fast signal processing capability. Based on this principle, a 12 GHz-bandwidth MWP radar with a range resolution of 1.3 cm [13] was established and inverse synthetic aperture radar (ISAR) imaging with a 2D resolution better than 2 cm × 2 cm [14], [15] was achieved. Besides, broadband phased-array radar and multiple-input-multiple-output (MIMO) radar were also demonstrated [16], [17]. These results can soundly verify the great potential of MWP techniques in radar applications.

In EW systems, fast and broadband frequency measurement of intercepted microwave signal from a radar or a communication system is of critical importance for threat warning and communication interception. Up to now, a number of frequency measurement approaches based on MWP techniques have been proposed, including frequency-to-power mapping method, frequency-to-space mapping method, and frequency-to-time mapping method [19]–[33], etc. The frequency-to-power mapping method is usually realized by constructing an amplitude comparison function (ACF), a relationship between the frequency of the signal under test (SUT) and the power

Manuscript received October 8, 2019; revised November 28, 2019; accepted January 6, 2020. Date of publication January 9, 2020; date of current version April 15, 2020. This work was supported in part by the NSFC program under Grant 61871214 and Grant 11804159, in part by the NSFC Program of Jiangsu Province under Grant BK20180066, in part by the Fundamental Research Funds for the Central Universities, under Grant NS2018028, in part by the Jiangsu Provincial "333" Project BRA2018042, in part by the Jiangsu Provincial Program for High-level Talents in Six Areas under Grant DZXX-005, and in part by the Postgraduate Research & Practice Innovation Program of Jiangsu Province, under Grant KYCX17_0289. *(Corresponding author: Fangzheng Zhang.)*

The authors are with the Key Laboratory of Radar Imaging and Microwave Photonics (Nanjing Univ. Aeronaut. Astronaut.), Ministry of Education, Nanjing University of Aeronautics and Astronautics, Nanjing 210016, China (e-mail: zhangfangzheng@nuaa.edu.cn).

Color versions of one or more of the figures in this article are available online at https://ieeexplore.ieee.org.

Digital Object Identifier 10.1109/JLT.2020.2965113

ratio of two optical or microwave channels [19]–[28]. In the frequency-to-space mapping method, the optical carrier is modulated by the SUT and then channelized to multiple channels, through which the frequency of the SUT can be estimated [29]–[31]. The frequency measurement can also be realized by frequency-to-time mapping [32], [33], e.g., the frequency was mapped to a certain time delay after transmission through an optical dispersive fiber [32]. Besides, the frequency can be measured through the phase slope recovered by broadband photonic frequency mixing [34].

To reduce the cost and volume of the hardware on platforms such as combat aircrafts, warships, and unmanned aerial vehicles (UAVs), incorporating radar and EW functions within a single system is highly desirable. For this purpose, the Office of Naval Research has initiated an Advanced Multifunction RF System (AMRFS) Program, aiming to realize the incorporation of shipboard RF functions using a common set of hardware [35]. Recently, we have integrated the radar imaging and frequency measurement functions within one electro-optical system in an optical frequency-division multiplexing manner [36]. In this system, the $\pm$ 1st-order and the 3rd-order LFM sidebands are separated and used for radar detection and frequency measurement, respectively. Thus, the radar transmit signal has a doubled bandwidth of the input LFM signal, and the frequency measurement range is triple of the bandwidth of the LFM signal. While, this scheme suffers from possible interference between the radar and frequency measurement functions, because the 1st-order and the 3rd-order LFM sidebands are difficult to separate due to the limited roll-off factor of current optical filters, especially when they are close or overlapped. This effect also limits the operation bandwidth of the system.

In this paper, we propose and demonstrate a photonics-based system for simultaneous radar detection and frequency measurement based on polarization-division multiplexing. The two functions are implemented by sharing a light with $\pm$ 2nd-order LFM sidebands, which is modulated by the radar echo and the signal under test (SUT) along two orthogonal polarizations at a dual-polarization Mach-Zehnder modulator (Dpol-MZM). Thanks to this polarization-division-multiplexing architecture, the optical modulation, transmission, amplification, and filtering can be implemented by a common set of optical devices, which helps to reduce the cost and the size of the system. Compared with the previous frequency-division multiplexing method, the proposed method here can effectively suppress the interference between the two functions. In addition, the use of $\pm$ 2nd-order LFM sidebands leads to a quadrupled bandwidth of the input LFM signal for both radar and frequency measurement applications, which is much enlarged than the operation bandwidth of the previous scheme. Furthermore, the proposed system has increased flexibility because its frequency measurement range can be reconfigured by simply adjusting the bias voltage of the electro-optical modulator.

This paper is organized as follows. In Section II, the principle of the proposed MWP system for simultaneous radar detection and frequency measurement is described. In Section III, experimental demonstration of the proposed system is carried out. Performances of the radar detection and the frequency measurement functions are investigated. In Section IV, the reconfigurablilty of the frequency measurement range, and the capability for measuring the frequency of wideband signal are demonstrated. Section V gives the conclusion.

## II. Principle

Fig. 1 shows the schematic diagram of the proposed system. A continuous-wave (CW) light with a frequency of $f_c$ is generated by a laser diode (LD). This light is modulated by a pair of electrical LFM signals when passing through a dual-parallel MZM (DPMZM). The two electrical LFM signals have a phase difference of $\pi/2$ between each other, and they are generated by an arbitrary waveform generator (AWG) together with an electrical 90 degree hybrid. The DPMZM consists of two sub-MZMs (MZMa and MZMb) in the two arms of a main MZM (MZMc). The two sub-MZMs are biased at the maximum transmission point (MATP) to suppress the odd-order modulation sidebands, and the main MZM (MZMc) is biased at the minimum transmission point (MITP) to suppress the optical carrier. Thus, the $\pm$ 2nd-order modulation sidebands dominate in the obtained spectrum (point a). The obtained optical signal after the DPMZM can be expressed as [12]

$$E_1(t) \propto J_2(\alpha)\left[e^{j2\pi(f_c+2f_{\mathrm{LFM}})t} + e^{j2\pi(f_c-2f_{\mathrm{LFM}})t}\right] \quad (1)$$

where $J_n(\cdot)$ is the $n$-th order Bessel function of the first kind, $\alpha$ is the modulation index, and $f_{\mathrm{LFM}} = f_0 + kt$ is the frequency of the LFM signals in a single period ($0 < t \leq T$) with $T$, $f_0$, $k$ being the temporal period, the initial frequency, and the chirp rate, respectively.

The optical signal from the DPMZM is divided into two parts through an optical coupler (OC). One part is injected into a photodetector (PD1) to generate the transmit signal expressed as

$$v_1(t) \propto \|E_1(t)\|^2 = 2J_2^2(\alpha)\cos\left[2\pi\left(4f_{\mathrm{LFM}}\right)t\right] \quad (2)$$

It can be seen that both the center frequency and the bandwidth of the transmit signal are quadrupled compared with those of the LFM signal from the AWG. This obtained signal is amplified by an amplifier (Amp1) and then launched to the air by the radar transmit antenna (Radar Tx).

The other part from the OC is injected into a Dpol-MZM, composed by two sub-MZMs (MZM1 in X-polarization, MZM2 in Y-polarization), a polarization rotator (PR), and a polarization beam combiner (PBC). Both MZM1 and MZM2 are biased at the quadrature point (QP). In X-polarization, MZM1 is driven by the radar echo, received by the radar receive antenna (Radar Rx) and amplified by an electrical amplifier (Amp2). In Y-polarization, MZM2 is driven by the SUT collected by another receive antenna for frequency measurement. Before applied to MZM2, the SUT is amplified by an amplifier (Amp3) and selected by an electrical band-pass filter (EBPF1). Here, EBPF1 is used to avoid the interference from the radar signal and the undesired image-frequency signal. To this point, the radar echo and the SUT are carried by the lightwaves along two orthogonal polarizations. The obtained polarization-division-multiplexed optical signal (point b) can be

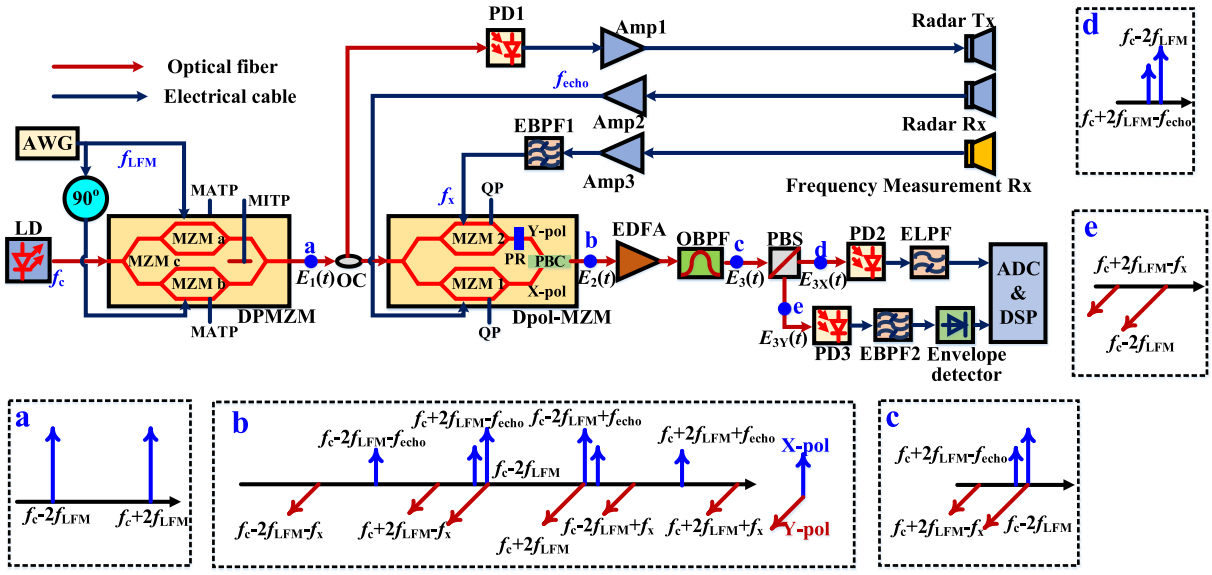


Fig. 1. Schematic diagram of the system for simultaneous radar detection and frequency measurement. AWG: arbitrary waveform generator; LD: laser diode; DPMZM: dual-parallel Mach–Zehnder modulator; MATP: maximum transmission point; MITP: minimum transmission point; OC: optical coupler; PD: photodetector; Amp: amplifier; EBPF: electrical band-pass filter; Dpol-MZM: dual-polarization MZM; PR: polarization rotator; PBC: polarization beam combiner; QP: quadrature point; EDFA: Erbium-doped fiber amplifier; OBPF: optical band-pass filter; PBS: polarization beam splitter; ELPF: electrical low-pass filter; ADC: analog-to-digital converter; DSP: digital signal processing.

expressed as

$$\mathbf{E_2}(t) \approx \hat{x}\frac{\sqrt{2}}{2}E_1(t)\left[J_0(\alpha_1) - J_1(\alpha_1)\left(e^{j2\pi f_{\text{echo}}t} + e^{-j2\pi f_{\text{echo}}t}\right)\right] + \hat{y}\frac{\sqrt{2}}{2}E_1(t) \times \left[J_0(\alpha_2) - J_1(\alpha_2)\left(e^{j2\pi f_x t} + e^{-j2\pi f_x t}\right)\right] \quad (3)$$

where $f_{\text{echo}}$ and $f_x$ are the frequencies of the radar echo and the SUT, respectively, and $\alpha_1$ and $\alpha_2$ are the modulation indexes of MZM1 and MZM2, respectively. In (3), only the optical carrier and the $\pm$ 1st sidebands are considered, considering the higher order sidebands have much smaller amplitudes.

After the Dpol-MZM, an Erbium-doped fiber amplifier (EDFA) is used to boost the optical power, and an optical band-pass filter (OBPF) is followed to select the three frequency components at $f_c$-2$f_{\text{LFM}}$, $f_c$ + 2$f_{\text{LFM}}$-$f_{\text{echo}}$, and $f_c$ + 2$f_{\text{LFM}}$-$f_x$ (point c). The obtained signal can be expressed as

$$\mathbf{E_3}(t) \propto \hat{x}\frac{\sqrt{2}}{2}J_2(\alpha)\begin{bmatrix} J_0(\alpha_1)\,e^{j2\pi(f_c-2f_{\text{LFM}})t} \\ -J_1(\alpha_1)\,e^{j2\pi(f_c+2f_{\text{LFM}}-f_{\text{echo}})t}\end{bmatrix} + \hat{y}\frac{\sqrt{2}}{2}J_2(\alpha)\begin{bmatrix} J_0(\alpha_2)\,e^{j2\pi(f_c-2f_{\text{LFM}})t} \\ -J_1(\alpha_2)\,e^{j2\pi(f_c+2f_{\text{LFM}}-f_x)t}\end{bmatrix} \quad (4)$$

Then, the signal in X-polarization and that in Y-polarization are separated by a polarization beam splitter (PBS) (points d and e). The obtained two optical signals are

$$E_{3X}(t) \propto \frac{\sqrt{2}}{2}J_2(\alpha)\begin{bmatrix} J_0(\alpha_1)\,e^{j2\pi(f_c-2f_{\text{LFM}})t} \\ -J_1(\alpha_1)\,e^{j2\pi(f_c+2f_{\text{LFM}}-f_{\text{echo}})t}\end{bmatrix} \quad (5)$$

$$E_{3Y}(t) \propto \frac{\sqrt{2}}{2}J_2(\alpha)\begin{bmatrix} J_0(\alpha_2)\,e^{j2\pi(f_c-2f_{\text{LFM}})t} \\ -J_1(\alpha_2)\,e^{j2\pi(f_c+2f_{\text{LFM}}-f_x)t}\end{bmatrix} \quad (6)$$

The signal in X-polarization carrying the radar echo information is sent to a PD (PD2) for optical-to-electrical conversion. An electrical low-pass filter (ELPF) is followed to select the de-chirped low frequency component, which is

$$v_2(t) \propto J_2^2(\alpha)\,J_0(\alpha_1)\,J_1(\alpha_1)\cos\left[2\pi\left(4f_{\text{LFM}} - f_{\text{echo}}\right)t\right] \quad (7)$$

In (7), the de-chirped signal has a frequency of $f_{\text{Ra}} = 4f_{\text{LFM}}$-$f_{\text{echo}}$. Assuming the received echo signal is delayed by $\tau$ compared with the transmitted signal, the de-chirped signal frequency would be $f_{\text{Ra}} = 4k\tau$ [12]. In the digital signal processing (DSP) unit, the frequency of the de-chirped signal can be acquired by simple spectral analysis of the signal sampled by a low-speed ADC, and the distance between the radar and target can be derived by

$$d = \frac{c\tau}{2} = \frac{cf_{\text{Ra}}}{8k} \quad (8)$$

where $c$ is the speed of electromagnetic propagation.

At the same time, the optical signal in Y-polarization is sent to another PD (PD3), from which the output electrical signal is

$$v_3(t) \propto J_2^2(\alpha)\,J_0(\alpha_2)\,J_1(\alpha_2)\cos\left[2\pi\left(4f_{\text{LFM}} - f_x\right)t\right] + \frac{1}{2}J_2^2(\alpha)\left[J_0^2(\alpha_2) + J_1^2(\alpha_2)\right] \quad (9)$$

The signal in (9) contains a dc component and a frequency component at $|4f_{\text{LFM}}$-$f_x|$. Following PD3, a narrow-band electrical band-pass filter (EBPF2) centered at $f_{\text{IF}}$ is connected. The spectrum of the output signal can be denoted by

$$S_E(f) \propto \left[\delta(f) + \delta\left(f - |4f_{\text{LFM}} - f_x|\right)\right]\delta\left(f - f_{\text{IF}}\right) = \delta\left(|4f_{\text{LFM}} - f_x| - f_{\text{IF}}\right)\delta\left(f - f_{\text{IF}}\right) \quad (10)$$

where $\delta(f) + \delta(f\text{-}|4f_{\mathrm{LFM}}\text{-}f_{\mathrm{x}}|)$ is the spectrum of $v_3(t)$, $\delta(f\text{-}f_{\mathrm{IF}})$ is the transfer function of EBPF2. Eq. (10) indicates that the obtained signal is an amplitude-modulated signal with a carrier frequency of $f_{\mathrm{IF}}$. When a microwave envelope detector is applied after EBPF2, the obtained signal can be derived as

$$e(t) = \delta\left(|4f_{\mathrm{LFM}} - f_{\mathrm{x}}| - f_{\mathrm{IF}}\right) = \delta\left(|4f_0 + 4kt - f_{\mathrm{x}}| - f_{\mathrm{IF}}\right) = \begin{cases} 1 & t = \frac{f_{\mathrm{x}}+f_{\mathrm{IF}}-4f_0}{4k} \text{ or } t = \frac{f_{\mathrm{x}}-f_{\mathrm{IF}}-4f_0}{4k} \\ 0 & \text{else} \end{cases} \tag{11}$$

As can be seen, the frequency under test ($f_{\mathrm{x}}$) is determined by the time when the output is nonzero, i.e., $e(t)\neq 0$. Based on (11), the frequency $f_{\mathrm{x}}$ can be estimated by

$$f_{\mathrm{x}} = 4kt_{\mathrm{I}} + 4f_0 - f_{\mathrm{IF}} \quad \text{or} \quad f_{\mathrm{x}} = 4kt_{\mathrm{I}} + 4f_0 + f_{\mathrm{IF}} \tag{12}$$

where $t_{\mathrm{I}}$ is the time when $e(t_{\mathrm{I}})\neq 0$. Since $t_{\mathrm{I}}$ changes from 0 to $T$, the frequency measurement range is from $4f_0$-$f_{\mathrm{IF}}$ to $4f_0$-$f_{\mathrm{IF}} + 4kT$, or from $4f_0 + f_{\mathrm{IF}}$ to $4f_0 + f_{\mathrm{IF}} + 4kT$. To avoid frequency overlapping between the two measurement ranges, $4f_0$-$f_{\mathrm{IF}} + 4kT < 4f_0 + f_{\mathrm{IF}}$ should be satisfied, requiring that the measurement bandwidth ($4kT$) should be less than $2f_{\mathrm{IF}}$. Besides, to solve the frequency measurement ambiguity problem, i.e., two image frequencies exists for a given time position in (12), an EBPF (EBPF1) with a specific pass band should be applied to confine the frequency measurement in the range of $4f_0$-$f_{\mathrm{IF}}$ to $4f_0$-$f_{\mathrm{IF}} + 4kT$, or $4f_0 + f_{\mathrm{IF}}$ to $4f_0 + f_{\mathrm{IF}} + 4kT$.

In the previous deduction, the optical devices are assumed to have ideal performance. In practical applications, polarization cross talk may occur due to the non-ideal separation of the optical signals in two polarizations after the PBS. Besides, the limited roll-off factor of the OBPF may induce spectral interference because the undesired modulation sidebands close to the required optical frequency components cannot be totally removed. These factors would degrade the signal to interference plus noise ratio (SINR), and thus reduce the dynamic range and deteriorate the sensitivity of the system. Therefore, an OBPF with large edge roll-off as well as PBS with high extinction ratio is preferred in the proposed system.

## III. Experimental Demonstration

To test the performance of the proposed system, an experiment is conducted based on the setup in Fig. 1. In the experiment, an LD (TeraXion PS-NLL) is used to generate the CW light source at 1550.126 nm with a power of 16 dBm. The light is modulated at a DPMZM (Fujitsu FTM7962EP) by a pair of LFM signals having a phase difference of $\pi/2$, of which the initial frequency, the bandwidth, and the temporal period are 4.5 GHz, 2 GHz, and 10 $\mu$s, respectively. The optical spectrum of the signal at the output of the DPMZM is measured by an optical spectrum analyzer (Yokogawa AQ6370C, Resolution: 0.02 nm) and shown in Fig. 2. As can be seen, the $\pm$ 2nd-order optical sidebands are generated with the optical carrier and other undesired sidebands well suppressed.

Following the DPMZM, a 3-dB OC is applied to split the optical signal into two branches. In one branch, the optical signal is injected into a PD (Optilab PD-30, Bandwidth: 30 GHz) to

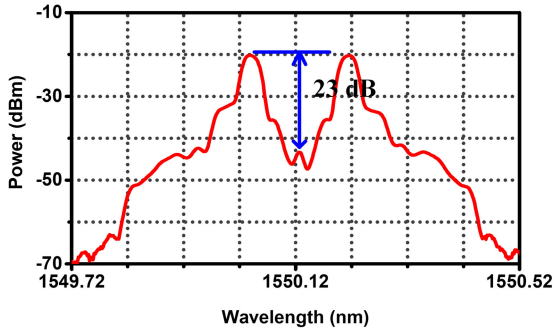


Fig. 2. Spectrum of the optical signal at the output of DPMZM.

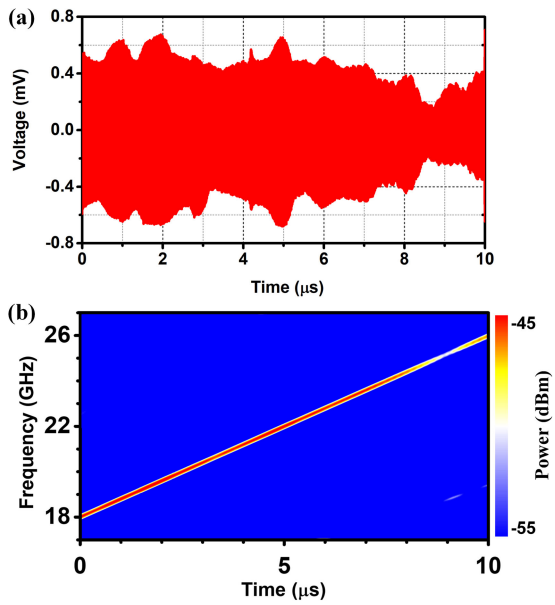


Fig. 3. (a) Time-domain waveform and (b) instantaneous frequency of the radar transmit signal.

generate the radar transmit signal. Fig. 3(a) shows the time-domain waveform of the radar transmit signal, which is observed by an 80-GHz real-time oscillator (Keysight DSO-X 92504A). Figure 3(b) illustrates the corresponding instantaneous frequency of the time-domain waveform. It can be seen that the frequency of the radar transmit signal increases from 18 to 26 GHz linearly in a period of 10 $\mu$s, indicating the transmit signal has a quadrupled bandwidth of the original LFM signal. This signal is amplified by an amplifier (A-INFOMW, bandwidth: 18–26.5 GHz, gain: 40 dB) and then is launched to the air through a K-band antenna. In the other branch of the OC, the optical signal is modulated at a Dpol-MZM (Fujitsu FTM7980EDA), where the sub-MZM in X-Polarization is driven by the radar echo signal and that in Y-Polarization is driven by the SUT. The SUT is generated by a commercial microwave signal generator (Keysight E8257D). As an example, the frequency of the SUT is set to 32 GHz. The blue line in Fig. 4(a) shows the spectrum of the optical signal at the output of the Dpol-MZM. An EDFA (Amonics AEDFA-35-B-FA) and an OBPF (Yenista XTM-50/S)

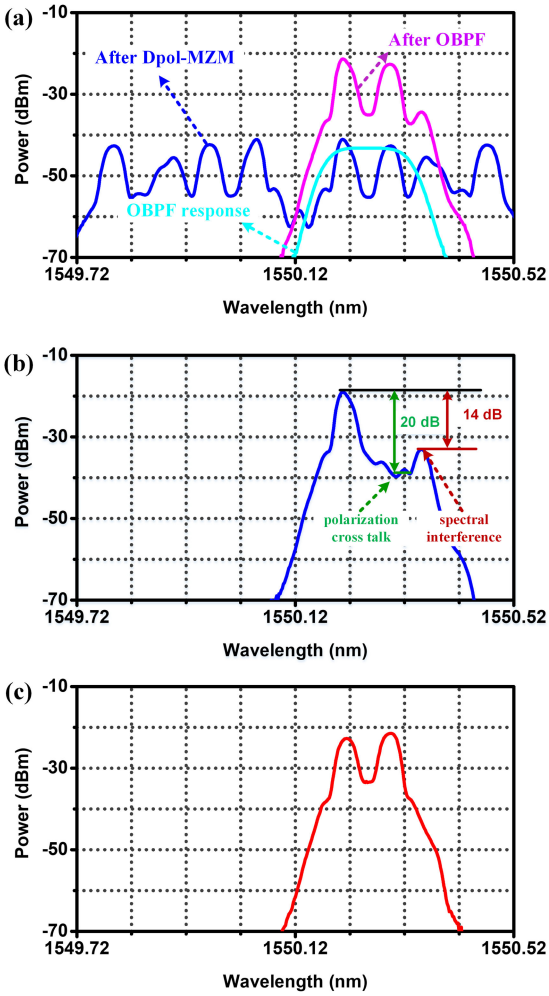


Fig. 4. Spectra of the optical signals (a) at the outputs of the Dpol-MZM and the OBPF, (b) at X-polarization port of the PBS, and (c) at Y-polarization port of the PBS.

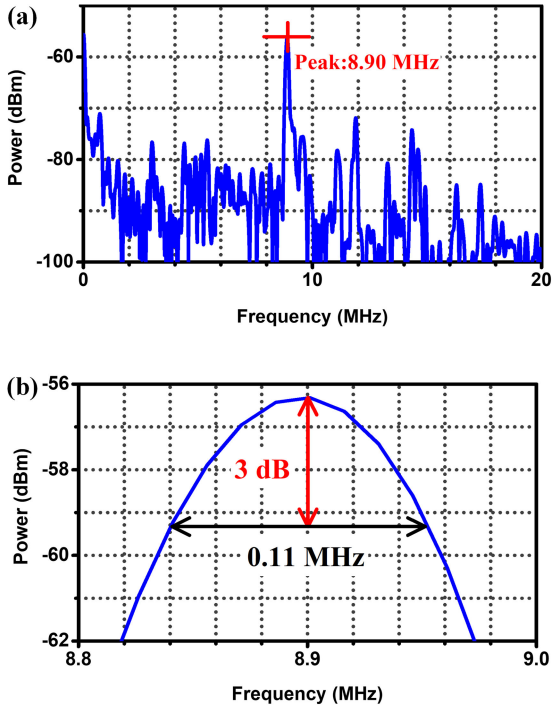


Fig. 5. (a) Frequency spectrum of the de-chirped signal and (b) zoom-in view of the spectrum around the peak.

are followed to amplify the optical signal and suppress the undesired sidebands, respectively. The response of the OBPF and the spectrum of the optical signal after the OBPF are also plotted in Fig. 4(a). Then, the signal in X-Polarization and that in Y-Polarization are separated by a PBS. The spectra of the signal in X-Polarization and that in Y-Polarization are shown in Fig. 4(b) and Fig. 4(c), respectively, through which the interferences caused by the unideal performance of the OBPF and PBS can be observed. In Fig. 4(b), the spectral interference caused by the modulation sideband at $f_c$-2$f_{\mathrm{LFM}}$-$f_{\mathrm{echo}}$ still exists, but has a power of 14 dB lower than the desired optical frequency components. The polarization cross talk can also be observed in Fig. 4(b). While, the optical components carrying the radar echo information has a power of 20-dB higher than that of the cross talk component.

Then, the signal in X-Polarization is sent to a PD (CETC44 GD45216S) with a 3-dB bandwidth of 18 GHz followed by an ELPF (Bandwidth: 20 MHz) to de-chirp the radar echo signal. The de-chirped signal is digitalized by a real-time oscillator (Keysight DSO-X 92504A) operating at a sampling rate of 100 MSa/s. The sampled data are sent to the DSP unit. In order to test the radar function, a metallic trihedral corner reflector (size: 2 cm × 2 cm × 2 cm) is used as the target, which is located about 1.65 m away from the antenna pair. Fig. 5(a) shows the spectrum of the de-chirped signal, of which the spectral peak appears at 8.90 MHz. According to (8), the distance between the target and the antenna pair is 1.67 m, which is very close to the real value. The range resolution of the radar function is also tested. Fig. 5(b) shows the zoom-in view of the spectral peak, in which the 3-dB bandwidth is 0.11 MHz, corresponding to a range resolution of 2.06 cm. Here, the measured range resolution is larger than the theoretical value of 1.875 cm for an 8 GHz-bandwidth radar [14]. This slight deviation is mainly caused by the fact that the target used in our experiment is not an ideal point target as its size is comparable with the radar resolution.

The signal in Y-Polarization is sent to another PD (CETC44 GD45216S) with a 3-dB bandwidth of 18 GHz followed by an EBPF (EBPF2) centered at 10 GHz with a 3-dB bandwidth of 15 MHz. An envelope detector (Agilent 8474C, Bandwidth: 0–33 GHz) is applied after the EBPF. The obtained signal is then recorded by the real-time oscillator working at a sampling rate of 100 MSa/s. According to (12), the frequency measurement range can be 28–36 GHz, or 8–16 GHz. The frequency measurement bandwidth is 8 GHz, which can be further improved by increasing the bandwidth of the input electrical LFM signal and the center frequency of EBPF2. To avoid the frequency measurement ambiguity, an EBPF is applied to enable a frequency measurement range of 28–36 GHz. Fig. 6 shows the waveform recorded by the oscillator when the frequency of the SUT is set

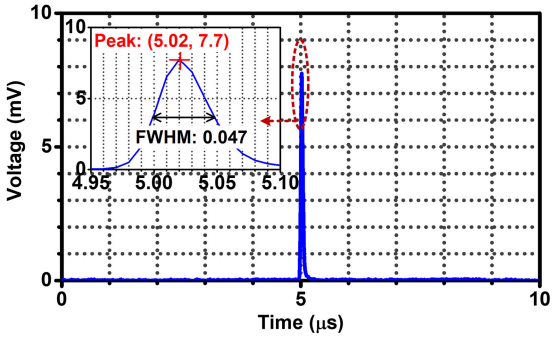


Fig. 6. Measured waveform when a 32-GHz signal is tested, and zoom-in view of the waveform around the pulse.

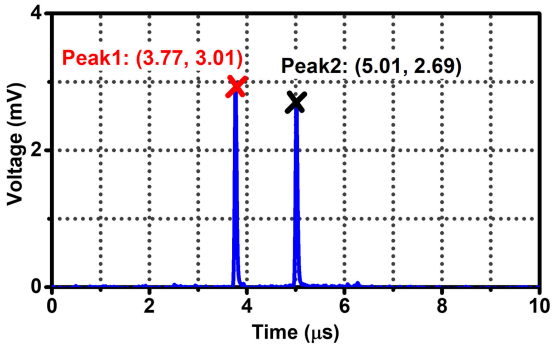


Fig. 7. Measured waveform when a two-tone signal with frequencies of 31 and 32 GHz is tested.

to 32 GHz. As we can see, a pulse appears at the time of 5.02 $\mu$s. According to (12), the frequency is estimated to be 32.016 GHz, corresponding to a measurement error of 16 MHz. From the zoom-in view of the pulse in Fig. 6, we can see the full width at half maximum (FWHM) of the pulse is 0.047 $\mu$s. Based on (12), a temporal interval of 0.047-$\mu$s corresponds to a frequency spacing of 37.6 MHz, thus, the frequency measurement resolution is 37.6 MHz. Ideally, the measurement resolution is determined by the 3-dB bandwidth of EBPF2 (15 MHz). However, in our experiment, the frequency scanning rate reaches as high as 0.8 GHz/$\mu$s. In this case, the temporal FWHM of the pulse is mainly determined by the rise-and-fall time ($2*0.35/B_{\mathrm{IF}}$) of EBPF2, where $B_{\mathrm{IF}}$ is the 3-dB bandwidth of EBPF2 [37].

In order to demonstrate the applicability of the frequency measurement function to multi-tone signals, a two-tone signal at 31 GHz and 32 GHz is acted as the SUT. Fig. 7 shows the corresponding waveform recorded by the oscillator. The two pulses appear at 3.77 and 5.01 $\mu$s, and the frequencies are estimated to be 31.016 and 32.008 GHz, respectively, which are very close to the real values. To test the measurement resolution, a two-tone signal with a 37.6-MHz frequency spacing (at 31.9624 GHz and 32 GHz) is measured with the results shown in Fig. 8. As can be seen, the two pulse peaks at 4.94 $\mu$s and 4.99 $\mu$s can be easily distinguished, indicating a frequency measurement resolution no more than 37.6 MHz is achieved.

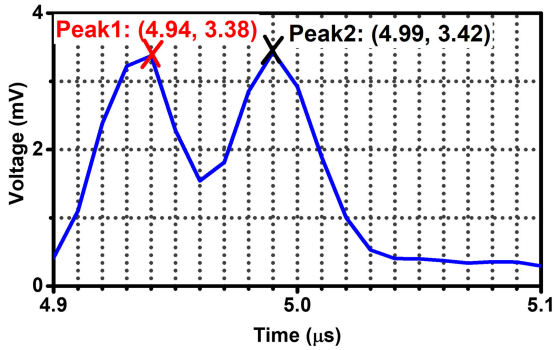


Fig. 8. Measured waveform when a two-tone signal with a frequency spacing of 37.6 MHz is tested.

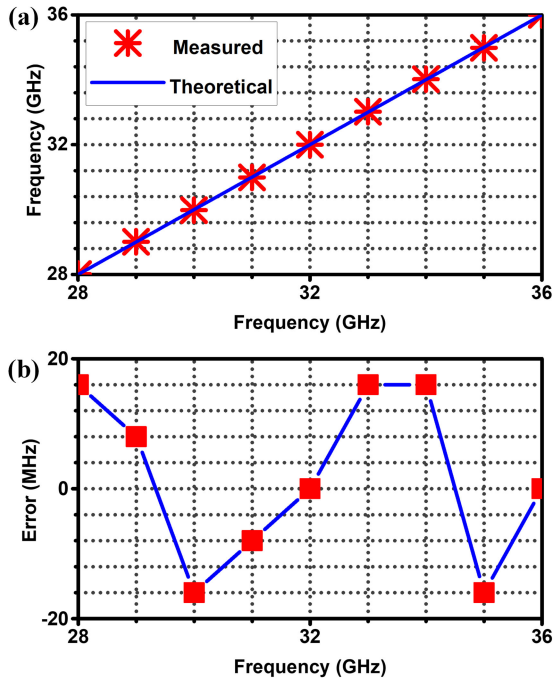


Fig. 9. (a) Measurement results when the frequency of the SUT is tuned from 28 to 36 GHz with a step of 1 GHz, and (b) measurement errors versus the input frequencies.

The frequency measurement errors are also investigated when measuring different frequencies. Fig. 9(a) shows the measurement results when the frequency of the SUT is tuned from 28 GHz to 36 GHz with a step of 1 GHz, and Fig. 9(b) shows the measurement errors. We can see that the errors are kept within $\pm$16 MHz in the whole frequency measurement range.

## IV. Discussion

In the proposed system, the frequency measurement range is changeable by simply tuning the bias voltage of MZM2 in the Dpol-MZM from the quadrature point (QP) to the minimum transmission point (MITP). When MZM2 is operated at the MITP, the illustrative spectra at point b, c and e in Fig. 1 are changed to the spectra in Fig. 10. Specifically, the optical signal

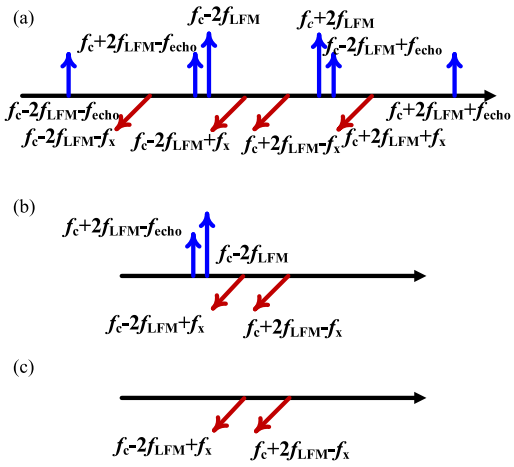


Fig. 10. Illustrative spectra at the output of Dpol-MZM (a) and OBPF (b), and at Y-polarization port of the PBS (c) when MZM2 is biased at the MITP.

at the output of the Dpol-MZM (point b) is

$$\begin{aligned}\mathbf{E_2'}(t) \approx \hat{x}\frac{\sqrt{2}}{2}E_1(t) \\ \times \left[J_0(\alpha_1) - J_1(\alpha_1)\left(e^{j2\pi f_{\text{echo}}t} + e^{-j2\pi f_{\text{echo}}t}\right)\right] \\ - \hat{y}E_1(t)\,J_1(\alpha_2)\left(e^{j2\pi f_x t} + e^{-j2\pi f_x t}\right)\end{aligned} \tag{13}$$

Then, OBPF2 is applied to select four frequency components at $f_c$-2$f_{\text{LFM}}$, $f_c + 2f_{\text{LFM}}$-$f_{\text{echo}}$, $f_c$-2$f_{\text{LFM}} + f_x$, and $f_c + 2f_{\text{LFM}}$-$f_x$. The obtained optical signal (point c) is

$$\begin{aligned}\mathbf{E_3'}(t) \propto \hat{x}\frac{\sqrt{2}}{2}J_2(\alpha)\begin{bmatrix}J_0(\alpha_1)\,e^{j2\pi(f_c-2f_{\text{LFM}})t} \\ -J_1(\alpha_1)\,e^{j2\pi(f_c+2f_{\text{LFM}}-f_{\text{echo}})t}\end{bmatrix} \\ + \hat{y}\frac{\sqrt{2}}{2}J_2(\alpha)\begin{bmatrix}J_1(\alpha_2)\,e^{j2\pi(f_c-2f_{\text{LFM}}+f_x)t} \\ -J_1(\alpha_2)\,e^{j2\pi(f_c+2f_{\text{LFM}}-f_x)t}\end{bmatrix}\end{aligned} \tag{14}$$

Comparing Eq. (14) with Eq. (4), it can be seen that the signal in X-polarization for radar detection remains unchanged. Thus, changing the bias voltage of MZM2 does not affect the radar function. When the signal in Y-polarization (point e) is sent to PD3, the obtained electrical signal is

$$\begin{aligned}v_3'(t) \propto J_2^2(\alpha)\,J_1^2(\alpha_2)\cos\left[2\pi\left(4f_{\text{LFM}} - 2f_x\right)t\right] \\ + J_2^2(\alpha)\,J_1^2(\alpha_2)\end{aligned} \tag{15}$$

This signal is filtered by EBPF2, of which the output is

$$\begin{aligned}S_{\text{E}}'(f) &\propto \left[\delta(f) + \delta\left(f - |4f_{\text{LFM}} - 2f_x|\right)\right]\delta\left(f - f_{\text{IF}}\right) \\ &= \delta\left(|4f_{\text{LFM}} - 2f_x| - f_{\text{IF}}\right)\delta\left(f - f_{\text{IF}}\right)\end{aligned} \tag{16}$$

After envelope detection, the obtained signal is

$$\begin{aligned}e'(t) &= \delta\left(|4f_{\text{LFM}} - 2f_x| - f_{\text{IF}}\right) \\ &= \delta\left(|4f_0 + 4kt - 2f_x| - f_{\text{IF}}\right) \\ &= \begin{cases}1 & t = \frac{2f_x + f_{\text{IF}} - 4f_0}{4k} \text{ or } t = \frac{2f_x - f_{\text{IF}} - 4f_0}{4k} \\ 0 & \text{else}\end{cases}\end{aligned} \tag{17}$$

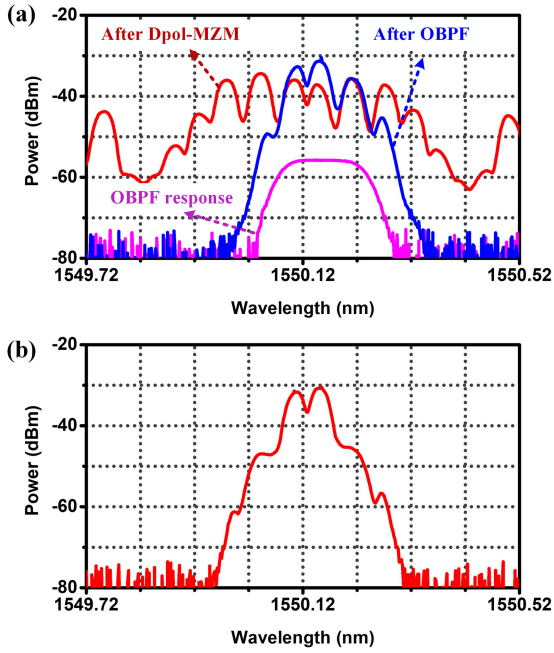


Fig. 11. Spectra of the optical signals (a) at the outputs of the Dpol-MZM and the OBPF, and (b) at Y-polarization port of the PBS.

Similar with the previous deduction, the frequency under test ($f_x$) becomes

$$f_X = 2kt_I + 2f_0 - \frac{f_{IF}}{2} \quad \text{or} \quad f_X = 2kt_I + 2f_0 + \frac{f_{IF}}{2} \tag{18}$$

According to (18), the frequency measurement range is from $2f_0$-$f_{\text{IF}}/2$ to $2f_0$-$f_{\text{IF}}/2 + 2kT$, or from $2f_0 + 2f_{\text{IF}}$ to $2f_0 + 2f_{\text{IF}} + 2kT$, which is different from the range when MZM2 is biased at the QP.

The feasibility of this method is tested with the previous experimental setup, in which the bias voltage of MZM2 is changed to the MITP. According to (18), the frequency measurement range is from 4 to 8 GHz, or from 14 to 18 GHz. In our experiment, frequency measurement in the range from 4 to 8 GHz is demonstrated. Fig. 11(a) shows the spectrum at the output of the Dpol-MZM, the response of the OBPF, and the spectrum of the signal after the OBPF when the SUT has a frequency of 6 GHz. The spectrum of the optical signal in Y-polarization is plotted in Fig. 11(b). Fig. 12 shows the waveforms after envelope detection when the frequency of the SUT is tuned from 4 to 8 GHz with a step of 1 GHz. According to the temporal positions of the pulses, the frequencies are measured to be 4.002, 5.018, 6.018, 6.986, 7.986 GHz, respectively, with the measurement errors less than 18 MHz.

Finally, measurement of the spectrum of a communication signal (carrier frequency: 6 GHz, quadrature phase shift keying modulation, symbol rate: 250 MBaud) is demonstrated by the established system with a frequency measurement range of 4–8 GHz. Fig. 13 shows the measured spectrum. It is shown that, the signal has a 3-dB bandwidth of 240 MHz, which is very close to the symbol rate. The result verifies the capability of the proposed system for measuring wideband signals.

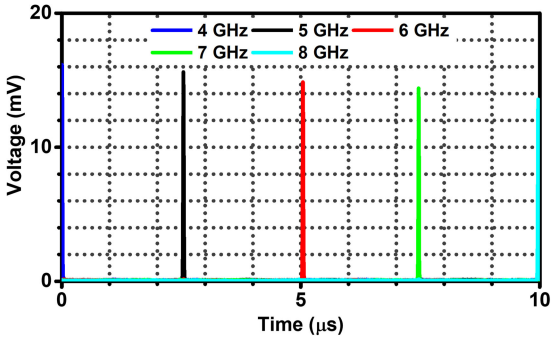


Fig. 12. Measured waveforms when the frequency of the SUT is tuned from 4 to 8 GHz with a step of 1 GHz.

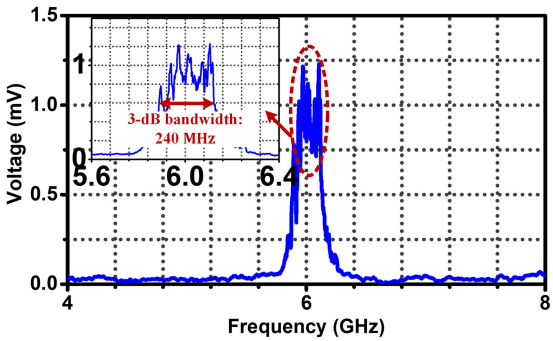


Fig. 13. Frequency measurement result of a communication signal with a carrier frequency of 6 GHz and a symbol rate of 250 MBaud.

## V. Conclusion

In this paper, we propose and demonstrate a microwave photonic system that can simultaneously realize broadband radar detection and frequency measurement. Thanks to the photonics-assisted frequency quadrupler, using a LFM signal with a bandwidth of 2 GHz and a temporal period of 10 $\mu$s, a transmit signal with a bandwidth of 8 GHz (from 18 to 26 GHz) is generated, which enables a range resolution as high as 2.06 cm, and an 8-GHz frequency measurement range from 28 to 36 GHz with a fast scanning rate of 0.8 GHz/$\mu$s is realized. By tuning the bias voltage of the Dpol-MZM, the frequency measurement range is reconfigurable. In addition, the applicability of the frequency measurement function to multi-tone and wideband signals is also demonstrated. The proposed system can find applications in the future electric systems, where broadband radar detection and frequency measurement are required.

## References

[1] J. Capmany and D. Novak, "Microwave photonics combines two worlds," *Nature Photon*., vol. 1, pp. 319–330, Jun. 2007.
[2] J. P. Yao, "Microwave photonics," *J. Lightw. Technol.*, vol. 27, no. 3, pp. 314–335, Feb. 2009.
[3] T. Berceli, and P. Herczfeld, "Microwave photonics - A historical perspective," *IEEE Trans. Microw. Theory Tech.*, vol. 58, no. 11, pp. 2992–3000, Nov. 2010.
[4] K. Xu *et al.*, "Microwave photonics: Radio-Over-Fiber links systems and applications," *Photon. Res.*, vol. 2, no. 4, pp. B54–B63, Aug. 2014.
[5] P. Ghelfi *et al.*, "Photonics in radar systems," *IEEE Microw. Mag*, vol. 16, no. 8, pp. 74–83, Sep. 2015.
[6] S. L. Pan and J. P. Yao, "Photonics-based broadband microwave measurement," *J. Light. Technol.*, vol. 35, no. 16, pp. 3498–3513, Aug. 2016.
[7] X. H. Zou, B. Lu, W. Pan, L. S. Yan, A. Stöhr, and J. P. Yao, "Photonics for microwave measurements," *Laser Photon. Rev.*, vol. 10, no. 5, pp. 711–734, Sep. 2016.
[8] P. Ghelfi *et al.*, "A fully photonics-based coherent radar system," *Nature*, vol. 507, pp. 341–345, Mar. 2014.
[9] W. Zou, H. Zhang, X. Long, S. Zhang, Y. Cui, and J. Chen, "All-optical central-frequency-programmable and bandwidth-tailorable radar," *Sci. Rep.*, vol. 6, p. 19786, Jan. 2016.
[10] S. Peng *et al.*, "High-resolution W-band ISAR imaging system utilizing a logic-operation-based photonic digital-to-analog converter," *Opt. Exp.*, vol. 26, pp. 1978–1987, 2018.
[11] R. Li *et al.*, "Demonstration of a microwave photonic synthetic aperture radar based on photonic-assisted signal generation and stretch processing," *Opt. Exp.*, vol. 25, no. 13, pp. 14334–14340, Jun. 2017.
[12] F. Z. Zhang, Q. S. Guo, and S. L. Pan, "Photonics-based real-time ultra-high-range-resolution radar with broadband signal generation and processing," *Sci. Rep.*, vol. 7, p. 13848, Oct. 2017.
[13] Y. Yao, F. Z. Zhang, Y. Zhang, X. W. Ye, D. Y. Zhu, and S. L. Pan, "Demonstration of ultra-high-resolution photonics-based Kaband inverse synthetic aperture radar imaging," in *Proc. Opt. Fiber Commun. Conf. Expo.*, San Diego, CA, USA, Mar. 2018, pp. 1–3.
[14] F. Z. Zhang *et al.*, "Photonics-based broadband radar for high-resolution and real-time inverse synthetic aperture imaging," *Opt. Exp.*, vol. 25, no. 14, pp. 16274–16281, Jul. 2017.
[15] F. Z. Zhang *et al.*, "Photonics-based real-time and high-resolution ISAR imaging of non-cooperative target," *Chin. Opt. Lett.*, vol. 15, no. 11, p. 112801, Nov. 2017.
[16] B. D. Gao, F. Z. Zhang, E. M. Zhao, D. C. Zhang, and S. L. Pan, "High-resolution phased array radar imaging by photonics-based broadband digital beamforming," *Opt. Exp.*, vol. 27, no. 9, pp. 13194–13203, Apr. 2019.
[17] F. Z. Zhang, B. D. Gao, and S. L. Pan, "Photonics-based MIMO radar with high-resolution and fast detection capability," *Opt. Exp.*, vol. 26, no. 13, pp. 17529–17540, Jun. 2018.
[18] X. W. Ye, F. Z. Zhang, Y. Yang, and S. L. Pan, "Photonics-based radar with balanced I/Q de-chirping for interference-suppressed high-resolution detection and imaging," *Photon. Res.*, vol. 7, no. 3, pp. 265–272, Mar. 2019.
[19] L. V. T. Nguyen and D. B. Hunter, "A photonic technique for microwave frequency measurement," *IEEE Photon. Technol. Lett.*, vol. 18, no. 10, pp. 1188–1190, May 2006.
[20] M. Attygalle and D. B. Hunter, "Improved photonic technique for broadband radio-frequency measurement," *IEEE Photon. Technol. Lett.*, vol. 21, no. 4, pp. 206–208, Feb. 2009.
[21] X. H. Zou and J. P. Yao, "An optical approach to microwave frequency measurement with adjustable measurement range and resolution," *IEEE Photon. Technol. Lett.*, vol. 20, no. 23, pp. 1989–1991, Dec. 2008.
[22] J. Li *et al.*, "Photonic-assisted microwave frequency measurement with higher resolution and tunable range," *Opt. Lett.*, vol. 34, no. 6, pp. 743–745, Mar. 2009.
[23] W. Li, N. H. Zhu, and L. X. Wang, "Brillouin-assisted microwave frequency measurement with adjustable measurement range and resolution," *Opt. Lett.*, vol. 37, no. 2, pp. 166–168, Jan. 2012.
[24] X. H. Zou, H. Chi, and J. P. Yao, "Microwave frequency measurement based on optical power monitoring using a complementary optical filter pair," *IEEE Trans. Microw. Theory Techn.*, vol. 57, no. 2, pp. 505–511, Feb. 2009.
[25] H. Chi, X. H. Zou, and J. P. Yao, "An approach to the measurement of microwave frequency based on optical power monitoring," *IEEE Photon. Technol. Lett.*, vol. 20, no. 14, pp. 1249–1251, Jul. 2008.
[26] X. H. Zou, S. L. Pan, and J. P. Yao, "Instantaneous microwave frequency measurement with improved measurement range and resolution based on simultaneous phase modulation and intensity modulation," *J. Lightw. Technol.*, vol. 27, no. 23, pp. 5314–5320, Dec. 2009.
[27] Z. Li, B. Yang, H. Chi, X. M. Zhang, S. L. Zheng, and X. F. Jin, "Photonic instantaneous measurement of microwave frequency using fiber Bragg grating," *Opt. Commun.*, vol. 283, no. 3, pp. 396–399, Feb. 2010.
[28] S. L. Pan and J. P. Yao, "Instantaneous microwave frequency measurement using a photonic microwave filter pair," *IEEE Photon. Technol. Lett.*, vol. 22, no. 19, pp. 1437–1439, Oct. 2010.
[29] S. T. Winnall, A. C. Lindsay, M. W. Austin, J. Canning, and A. Mitchell, "A microwave channelizer and spectroscope based on an integrated optical Bragg-grating Fabry–Pérot and integrated hybrid Fresnel lens system," *IEEE Trans. Microw. Theory Techn.*, vol. 54, no. 2, pp. 868–872, Feb. 2006.

[30] L. X. Wang, N. H. Zhu, W. Li, H. Wang, J. Y. Zheng, and J. G. Liu, "Polarization division multiplexed photonic radio-frequency channelizer using an optical comb," *Opt. Commun.*, vol. 286, pp. 282–287, Jan. 2013.

[31] J. M. Heaton *et al.*, "Sixteen channel (1 to 16 GHz) microwave spectrum analyzer device based on a phased array of GaAs/AlGaAs electro-optic waveguide delay lines," *Proc. SPIE*, vol. 3278, pp. 245–251, Jan. 1998.

[32] L. V. T. Nguyen, "Microwave photonic technique for frequency measurement of simultaneous signals," *IEEE Photon. Technol. Lett.*, vol. 21, no. 10, pp. 642–644, May 2009.

[33] T. A. Nguyen, E. H. W. Chan, and R. A. Minasian, "Instantaneous high resolution multiple-frequency measurement system based on frequency-to-time mapping technique," *Opt. Lett.*, vol. 39, no. 8, pp. 2419–2422, Apr. 2014.

[34] J. Z. Shi, F. Z. Zhang, D. Ben, and S. L. Pan, "Photonics-based broadband microwave instantaneous frequency measurement by frequency-to-phase-slope mapping," *IEEE Trans. Microw. Theory Techn.*, vol. 67, no. 2, pp. 544–551, Feb. 2019.

[35] P. K. Hughes and J. Y. Choe, "Overview of advanced multifunction RF system (AMRFS)," in *Proc. IEEE Int. Conf. Phased Array Syst. Technol.*, May 2000, pp. 21–24.

[36] J. Z. Shi, F. Z. Zhang, X. W. Ye, Y. Yang, D. Ben, and S. L. Pan, "Photonics-based dual-functional system for simultaneous high-resolution radar imaging and fast frequency measurement," *Opt. Lett.*, vol. 44, no. 8, pp. 1948–1951, Apr. 2019.

[37] C. Mittermayer and A. Steininger, "On the determination of dynamic errors for rise time measurement with an oscilloscope," *IEEE Trans. Instrum. Meas.*, vol. 48, no. 6, pp. 1103–1107, Dec. 1999.